

Key building blocks of a silicon photonic integrated transmitter for future detector instrumentation¹

Y. Zhang,² M. Schneider, D. Karnick, L. Eisenblätter, T. Kühner and M. Weber

*Karlsruhe Institute of Technology, Institute for Data Processing and Electronics,
Hermann-von-Helmholtz-Platz 1, 76344 Eggenstein-Leopoldshafen, Germany,*

E-mail: zhang.yunlong@partner.kit.edu

ABSTRACT: The data throughput of future detector readout systems is ever increasing. We propose a high-performance optical link, based on silicon photonics and wavelength-division multiplexing (WDM) technology, to cope with ultra-broad bandwidth requirements. The key components of the proposed optical link are monolithically integrated transmitter units, each one integrating multi-channel on-chip Echelle grating (de-)multiplexers and Mach-Zehnder modulators (MZMs).

In our current design, each transmitter unit consists of four MZMs, which corresponds to four transmission channels with distinct optical carrier wavelengths, a common optical demultiplexer and a common optical multiplexer. In this paper, we present the design and experimental results of all these building blocks as well as a first transmission experiment. Additionally, experimental results of a thermal modulator to be used in a future design for working point control are presented.

KEYWORDS: Optical detector readout concepts; Data acquisition concepts

¹This article is an updated version of Y. Zhang, *Concept, design and verification of components for an integrated on-detector silicon photonic multichannel transmitter* in proceedings of *Topical Workshop on Electronics for Particle Physics (TWEPP2018)* PoS(TWEPP2018)057, DOI: <https://doi.org/10.22323/1.343.0057>.

²Corresponding author.

1 Introduction

The number of detector channels is increasing remarkably in high energy physics and photon science and in future detector systems it may reach many millions, even many billions of channels [1]. Consequently, huge amounts of raw data will be generated per second [2]. One intuitive solution to read out the data is data compression. However, even when compressing the data significantly, current optical links still cannot handle transmission on this scale. Improving the transmission bandwidth is a promising alternative solution and is becoming more and more attractive for detector instrumentation.

Optical links in state-of-the-art detector systems are implemented based on vertical cavity surface emitting lasers (VCSEL) [3, 4], where the information is encoded onto the optical carrier by varying the laser current. With this method, a data rate of 10 Gbit/s per fiber is achieved. Faster prototypes are under development, while the modulation speed is limited to several tens of gigabits per second per fiber since one fiber merely conveys one modulated signal. More importantly, VCSELs will not be able to withstand the expected radiation levels in the innermost regions of future HEP experiments according to the research from CERN [5, 6].

We are currently working on a novel solution based on silicon photonics and WDM technology to address the challenge of high-level irradiation and high bandwidth [7, 8]. As shown in figure 1, in our scheme the laser sources are located outside of the detector in areas with negligible radiation. A number of stabilized wavelength carriers from the lasers are combined by optical multiplexers to be transmitted over a common single mode glass fiber (SMF) to the transmitter units on a photonic chip inside the detector [9]. On chip, the optical carriers are separated by wavelength through an Echelle grating demultiplexer and forwarded to a number of Mach-Zehnder modulators (MZMs). Electrical signals from the sensor elements are pre-processed, mapped to available transmitter channels and amplified to the required levels to drive the electro-optic MZMs. The modulated optical signals are combined by a second Echelle grating multiplexer and transmitted to the counting room through a

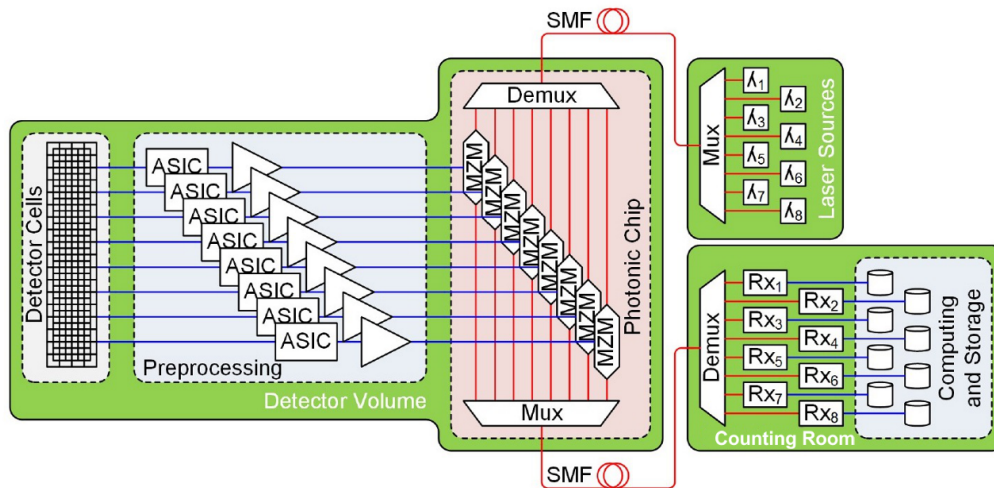


Figure 1. Concept of our WDM system for detector instrumentation. Multiple distinct optical carriers are combined on one fiber (top right). The photonic chip in the detector volume separates the incoming carriers, modulates them by electrical signals via MZMs and combines them again. The incoming data from the detector (left) are pre-processed and amplified before being transmitted to the photonic chip. Outgoing optical data are received in the counting room (bottom right).

common SMF. There, the signals are demultiplexed again and fed into individual receivers. The photonic chip inside the detector volume will be completely customized and tailored to the requirements, while the off-detector components are commercial off-the-shelf products to lower development costs.

2 Integrated 4-channel WDM transmitter units

Figure 2 is the photograph of our $9.2 \times 9.2 \text{ mm}^2$ photonic chip, which includes four WDM transmitter units (right side, see description below), Mach-Zehnder modulators with different lengths and structures (top-left quarter), Echelle grating demultiplexers and thermal modulators (bottom-left), as well as some other test structures. All components on this chip were designed to operate with TE polarized light. This chip was fabricated at IMS Chips (Institut für Mikroelektronik Stuttgart, Germany) on a 250 nm SOI platform. The top crystalline silicon layer is 250 nm thick, the buried silicon dioxide $2 \mu\text{m}$, and the silicon wafer $750 \mu\text{m}$. The strip waveguides are designed to be 500 nm wide to achieve single-mode and low-loss optical transmission.

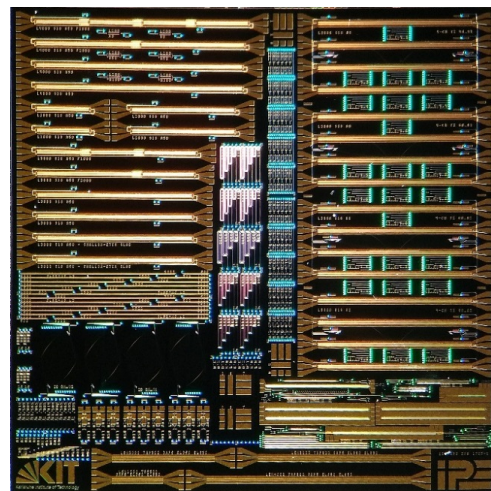


Figure 2. Photograph of photonic system chip ($9.2 \times 9.2 \text{ mm}^2$) with 4-channel WDM systems, single MZM, thermal modulators, Echelle gratings, and test structures.

The layout of a single WDM transmitter unit is illustrated in figure 3. Each WDM transmitter unit is composed of four MZMs (white coplanar horizontal stripes with tapers at their ends), one Echelle grating demultiplexer (green, center left), one mirrored Echelle grating multiplexer (green, center right) and several grating couplers. All transmitter units have an identical footprint of $3.8 \times 1.67 \text{ mm}^2$ and identical design parameters except that two of them

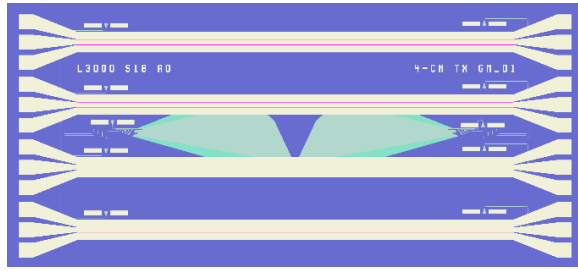


Figure 3. Layout of an on-chip 4-channel WDM transmitter unit.

employ 1×7 (de-)multiplexers and the other two employ 1×9 (de-)multiplexers. In reality, merely 4 channels of demultiplexers are in use for the transmitter units. The MZMs use two 2×2 3 dB multimode interferometers (MMIs) as optical splitters and combiners, namely each MZM has 2 inputs and 2 outputs. One MZM input is connected to the demultiplexer and one MZM output is connected to the multiplexer. The residual ports are connected to grating couplers for characterizing the modulators separately. Several test structures were placed between the MZMs of the transmitter units to make full use of the on-chip resource as shown in figure 2, while they are omitted in figure 3.

3 Key components for the transmitter unit

3.1 Carrier-depletion MZM

High-performance photonic modulators are key components for active silicon photonics. In the past decade, researchers have developed several kinds of modulators, such as the ring-resonator modulators, electro-absorption modulators and MZM modulators [10]. Ring-resonator modulators are strongly temperature dependent and usually an additional temperature controller is required to stabilize their characteristics. Electro-absorption modulators are based on advanced silicon-germanium fabrication technologies and are narrow-band in terms of operating wavelength. In comparison, carrier-depletion MZM modulators are mature and broadband in terms of operating wavelengths, which makes them suitable for WDM setups. More importantly, customized MZMs show favorable performance in terms of irradiation hardness [6].

Our MZM modulators consist of an optical power splitter, two phase shifters using the plasma dispersion effect and carrier-depletion [11], and an optical power combiner as shown in figure 4. With the merits of low loss and broad bandwidth, two 3-dB multimode interferometers are used as power splitter and combiner in our design [12], respectively.

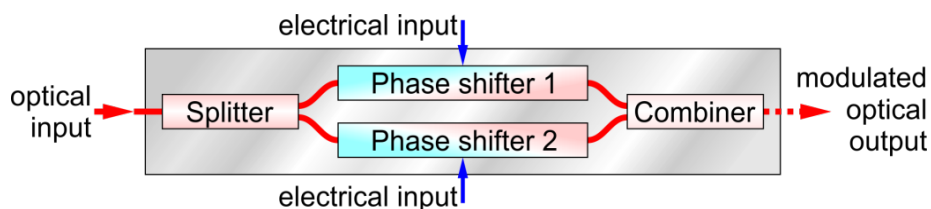


Figure 4. Schematic of an MZM modulator.

Figure 5 shows a simplified cross-section of a pn-phase shifter as used in our MZMs. The rib region is 500 nm wide and 250 nm thick, respectively. The buried oxide is approximately 2 μm thick, the SiO_2 top cladding, which is not shown in the schematic view, is 1 μm thick. The thickness of the slabs for electrical contacting is 120 nm i.e. the etching depth is 130 nm. We also developed another design with a shallower etch depth of 70 nm, resulting in a 180 nm thick slab. This design was driven by the study from Kraxner et al. in [6], who present two kinds of modulators based on a 220 nm SOI platform. The modulation efficiency of their deep etched modulators with 60 nm thick slabs decreased to 50% of its pre-irradiation value at a TID of 70 kGy. In comparison, their shallowly etched modulators with 150 nm thick slabs just started to degrade at 500 kGy TID. To be able to study the influence of the etching depth on the radiation hardness of our MZMs, we included above mentioned two designs for irradiation experiments in the future.

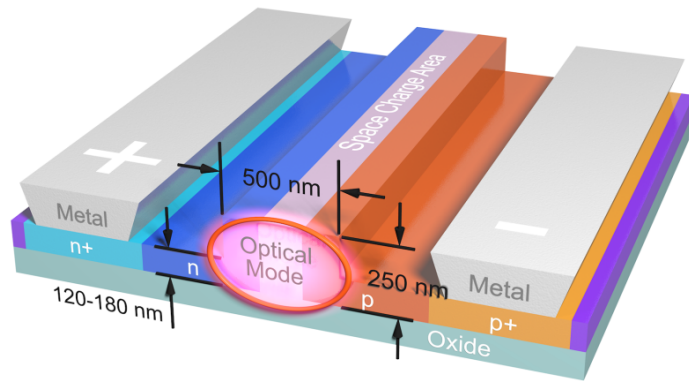


Figure 5. Schematic view of a pn-phase shifter.

The p and n regions of the modulators are doped symmetrically from the center of the rib to the sides with a doping concentration of $6.5 \times 10^{16} \text{ cm}^{-3}$, which is about half of the intended value of $1.5 \times 10^{17} \text{ cm}^{-3}$. A very first version of the chip suffered from an even lower doping concentration of just $1.5 \times 10^{16} \text{ cm}^{-3}$. Further away from the rib and under the metal contacts, highly doped p+ and n+ regions are fabricated for lower electrical resistance and better electrical connecting. Electrically, a coplanar transmission line is implemented with the two phase shifters of the MZM in the 5 μm wide gaps between the central conductor and the outer conductors. By linking the anode of one phase shifter and the cathode of the other one through the center conductor, a push-pull configuration is achieved for the phase shifters while applying a single-ended electrical signal (further discussed in 3.1.2 and shown in figure 8).

3.1.1 DC performance of the MZM

The modulators in the integrated WDM transmitter units have a length of 3 mm. To study the modulation efficiency, individual modulators with lengths of 1 mm, 2 mm, 3 mm, and 4 mm are included as well. These individual MZMs feature asymmetric arm lengths for easier characterization. DC characterization is performed by coupling light into the modulator from a tunable continuous wave laser source (Agilent 81689A) at a power of 6 dBm. To maintain a TE polarization, the light passes a polarization controller before entering the chip. The optical output of the modulator is coupled back into

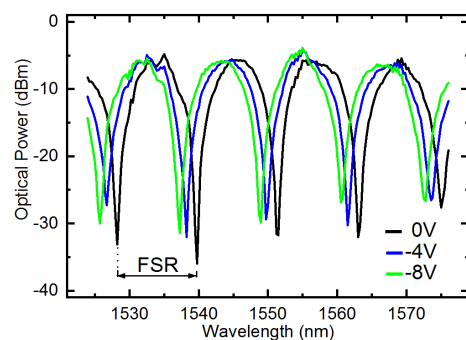


Figure 6. Transmission spectra of an asymmetric MZM with 3 mm long phase shifters at various bias voltages applied to one arm.

an SMF and measured by an optical power meter (Agilent 81623B and 81618A in an 8163B Light-wave Multimeter). Figure 6 shows the measured output spectra from an asymmetric 3 mm long MZM. The measured free spectral range (FSR) is 11.5 nm. A wavelength shift of 1.5 nm can be achieved by applying a reverse voltage of 4 V. According to relationship (3.1), a $V_{\pi}L_{\pi}$ of 4.6 V·cm can be derived.

$$\Delta\Phi = \frac{2\pi \cdot \Delta\lambda}{FSR} \quad (3.1)$$

The insertion loss of the 3 mm MZM is 4.84 dB when the MZI is in its on state, where maximum optical transmission occurs. This value is obtained by extracting the loss from two grating couplers and a waveguide with the length of the feed waveguides between grating couplers and MMIs. The currently used focusing grating couplers are not optimized and introduce an insertion loss of 5 dB each. Optimized couplers with aperiodic gratings and backside metal mirrors can achieve a much better coupling efficiency of about -0.6 dB [13, 14]. As the grating couplers are polarization sensitive, a polarization controller is used for individual modulator measurements. For a WDM system, operating with several optical carriers, this method is not a solution. Here either the polarization can be maintained by using polarization maintaining fibers or polarization insensitive coupling methods can be used. Currently, the former method is used, but for the final system, the latter one seems to be more feasible, but requires significant design efforts.

The same measurements were carried out for the modulators with the remaining lengths (1 mm, 2 mm, and 4 mm) and a plot of the phase shift versus bias voltage is given in figure 7. It is easily noticed that the phase shift increases monotonically with the bias voltage as well as with the length. One would expect equally spaced curves, but it can be seen that the green curve for the 3 mm long modulator is slightly shifted to higher values, presenting a higher efficiency. As the values scatter quite much due to either imperfect wafer quality or fabrication variations, this seems to be in the tolerances. In addition to the phase shift the insertion loss increases with modulator length. E.g. the 2 mm long modulator has an insertion loss of 4.56 dB while the 3 mm long modulator has a higher value of 4.84 dB. Therefore the optimal modulator length has been chosen based on multiple considerations.

3.1.2 Dynamic performance of the MZM

The high-speed performance of the MZM modulators was characterized by measuring both the frequency characteristics and the data transmission capacity of 3 mm long asymmetric and symmetric modulators. The symmetric modulators are part of the integrated WDM transmitters, but were characterized here without the Echelle grating multiplexers. To this end, the RF signal is generated either by a Rohde & Schwarz SMB100A microwave signal generator, or, for the data transmission

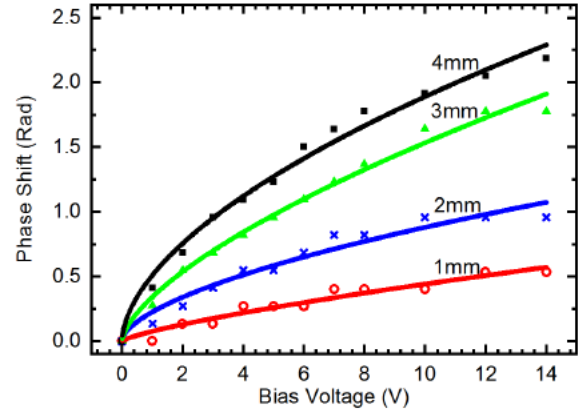


Figure 7. Phase shift versus bias voltage on one arm of an individual p-n junction phase shifter at different device lengths.

experiments, by an Altera Stratix V GX Transceiver Signal Integrity Development board, generating a pseudo-random bit sequence (PRBS). Reverse bias voltages and the RF signal were applied by special coplanar probe tips with separated outer conductors. The general electrical wiring of the setup is shown in figure 8, where one can observe the inherent push-pull configuration of our wiring method.

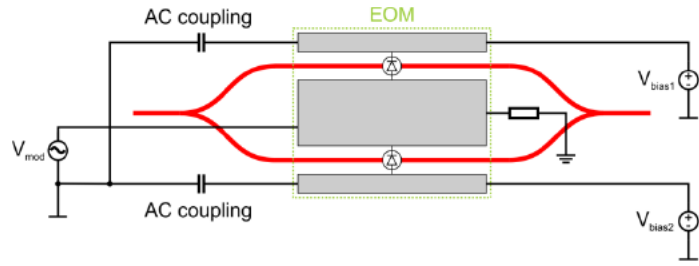


Figure 8. Electrical wiring of MZM for RF measurements and data transmission experiments.

The optical carrier was generated by the already mentioned tunable laser. The optical output of the modulator under test was routed to a photodiode (Newport AD-50xr), connected to an electrical spectrum analyzer (Rohde & Schwarz FSW43). With this setup the electrical→optical→electrical (EOE) response can be measured, which shows the performance of the electro-optic device, measured with an opto-electric converter (photodiode) in the electrical domain (electrical spectrum analyzer).

Both modulator arms of the asymmetric MZM were reversely biased at a voltage of 2.5 V. The optical input power to the device was fixed to +6 dBm, the average optical output power at the working point was about -14 dBm. The working point could be set by changing the laser wavelength, as the two MZM arms have different lengths. The signal generator frequency was swept from 100 MHz to 17 GHz. The result was corrected for cable losses and photodiode response and is shown in figure 9.

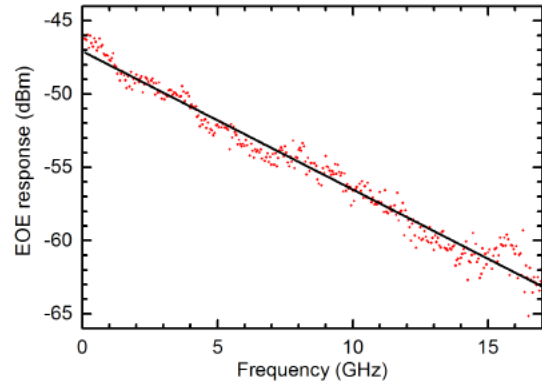


Figure 9. Frequency response of a normal etched, asymmetric MZM with 3 mm long phase shifters.

The curve shows a linear decrease with a slope of 0.76 dB/GHz and a 3 dB cut-off frequency of 3.28 GHz. The dominant reason for the low cut-off frequency might be the aforementioned fabrication error, i.e. the undesired low doping. Additionally, an impedance mismatch between transmission line (25Ω), generator, and load resistance (both 50Ω) also contributes to this result.

The data transmission capacity of the fabricated devices was characterized by measuring the bit error rate and the eye pattern. For these experiments the optical output signal from the modulator was amplified by an EDFA to an average power of 0 dBm. The photodiode was replaced by the receiver side of a commercial 1550 nm SFP+ module for 10 Gb/s transmissions in the C-band (Fiberstore SFP-10GER-55). The module was plugged into a breakout board with SMA connectors (Hitech Global HTG-SFP-SMA) and connected either to a fast sampling oscilloscope or to the FPGA board, which also generates the PRBS-7 bit sequence, for bit error rate measurements. For each pn-phase shifter in the MZM the reverse bias voltage was set to 2.5 V.

To get an overview, we measured the eye diagram with various settings for the driver and FPGA output circuitry. Due to the low 3 dB-cut-off frequency, the FPGA has to output its signal with a

significant pre-emphasis (setting 17 in the software out of a range from 0 to 31). The FPGA output signal was amplified by a two-stage amplifier consisting of two Hittite HMC870 evaluation boards to obtain a possible maximum output signal of 7 V (peak-to-peak).

Figure 10 shows an eye diagram of an asymmetric MZM with deep etched slabs at a data rate of 10 Gb/s. The peak-to-peak voltage of the modulator input signal was 6.0 V. Due to the impedance mismatch between measurement system and MZM, the modulator actually just ‘sees’ 65% of the voltage swing, which is 3.9 V. Nevertheless, the eye still remained open even for a measurement duration of several hours.

Connecting the receiver of the SFP+ module to the FPGA, we performed another set of bit error rate (BER) measurements, for which we were able to increase the data rate to 11.3 Gb/s. Figure 11 shows the measured bit error rate over the applied peak-to-peak voltage of the input signal. It can be seen that the data transmission using the shallow etched MZMs (open circles) remains error free for peak-to-peak voltages above 2.5 V. In comparison, the deep etched modulators (crosses) achieved a nearly error-free transmission at peak-to-peak voltages above 3.0 V. But the BER cannot be decreased down to 0 even if the voltage swing is further increased. This is induced by an EMC problem instead of the modulator design itself, as we observed error burst in intervals shorter than the measurement duration. These results show that modulator drivers with lower than expected peak-to-peak driving voltage can be used for high speed transmissions. The voltages are low enough to make a silicon based driver ASIC feasible. Another advantage of the reduced driving voltages is a greatly reduced power demand, as most of the RF signal is dissipated in the 50 Ω load resistor at the end of the MZM transmission line.

We also performed measurements on symmetric modulators of the integrated WDM transceivers. To set their working point, one bias voltage has to be increased significantly, deteriorating their modulation efficiency, as can be seen from the flattening curves in figure 7. With these modulators, the EOE response is similar to that of the asymmetric MZM, but about 10 dB lower. The lowest measured BER was 10^{-11} at a peak-to-peak driving voltage of 7 V. This shows that a working point control with additional phase shifters, preferably low loss thermal phase shifters as presented in section 3.3, in the MZM arms is inevitable.

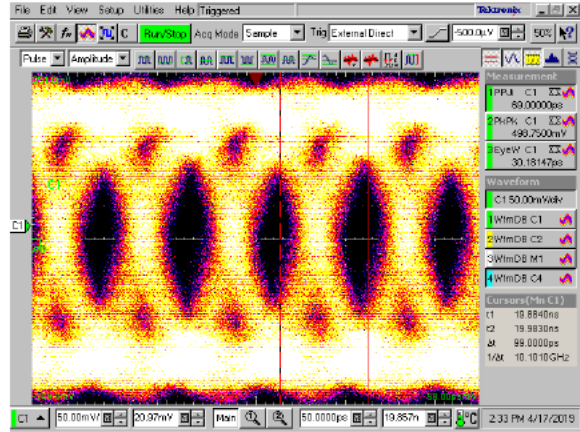


Figure 10. Bit error rates of deep etched and shallow etched MZM over the input voltage swing at 11.3 Gb/s.

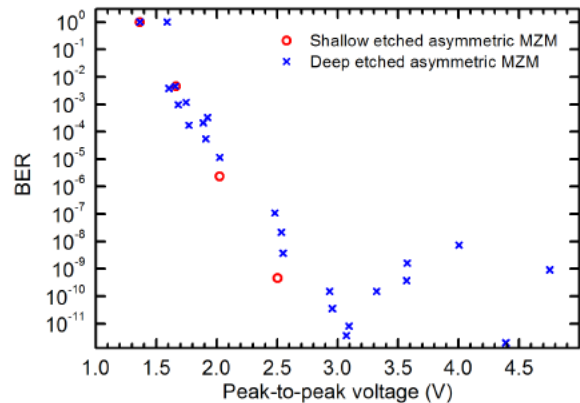


Figure 11. Eye diagram of an asymmetric, deep etched 3 mm MZM at a data rate of 10 Gb/s.

3.2 Echelle grating (de-)multiplexer

Besides the modulators the wavelength multiplexers and demultiplexers are key components for an on-chip WDM system. Two kinds of (de-)multiplexers were frequently investigated in the SOI platform, namely the arrayed waveguide gratings (AWG) and the Echelle grating (de-)multiplexers [15, 16]. Compared to AWG, Echelle gratings are more tolerant to edge roughness and feature a more compact on-chip footprint. The Echelle gratings presented in this paper are constructed using the Rowland circle method [17].

Figure 12 shows a schematic drawing of an Echelle grating for monolithic integration. At the lower left an input waveguide for a mix of different wavelength channels is located. The light is routed to a free space region, diverges and illuminates a concave grating at the top of the figure. The grating itself is constructed from elements which are in turn Bragg gratings as reflectors. Additionally the elements are tilted to make a blazed grating for higher efficiency. The light reflected from the concave grating is diffracted and, depending on the respective wavelength, focused to different positions where output waveguide ports are located, in the schematic figure four of them (lower right). In the other way around, the device works as wavelength multiplexer. In our integrated designs the waveguide ports are adiabatic tapers diverging from the already mentioned 500 nm waveguide width to 2 μm port width over a length of 30 μm . To avoid crosstalk induced by stray light and undesired multiple reflections, the borders of our devices feature highly n-doped regions, which serve as absorbers.

On our photonic chip of figure 2, two sets of Echelle grating (de-)multiplexers are employed by the transmitter units, which are 9-channel (1×9) and 7-channel (1×7) devices, respectively. For the 4-channel WDM-system, only every other channel of the constructed (de-)multiplexers is used. Figure 13 shows a basic Rowland mounting and the relevant design parameters. The required

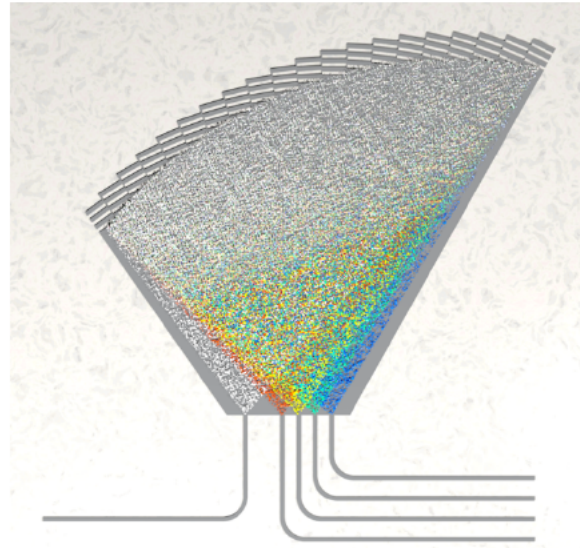


Figure 12. Schematic drawing of a monolithically integrated Echelle grating (de-)multiplexer.

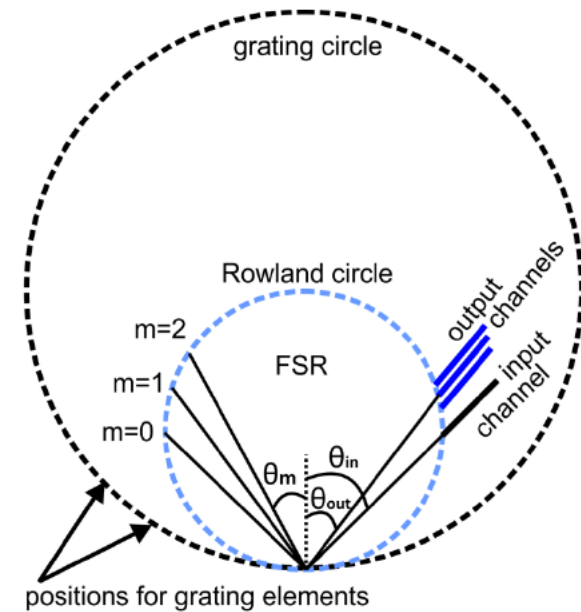


Figure 13. Rowland circle design method and parameter description.

parameters to construct the 1×9 Echelle grating (de-)multiplexer are channel spacing (3.19 nm), diffraction order ($m = 9$), radius of the Rowland circle (600 μm), length of grating (500 μm), input angle ($\theta_{\text{in}} = 53^\circ$) and central output angle ($\theta_{\text{out}} = 51^\circ$). By using these design parameters, we got a layout with an on-chip dimension of $1350 \times 670 \mu\text{m}^2$. The 1×7 Echelle grating (de-)multiplexers are designed identically except that the two outer channels were omitted.

Using the abovementioned tunable laser source, we measured the transmission spectra of each channel for the 1×9 (de-)multiplexer for wavelengths from 1524 nm to 1576 nm. The results are shown in figure 14. The average optical loss is approximately 4 dB and the maximum crosstalk between adjacent channels is -15 dB. Since we use every other channel in our WDM system, the crosstalk is effectively reduced to -20 dB. The center wavelength (1540.5 nm) deviates 5.6 nm from the design value of 1546.1 nm due to deviations in wafer thickness. Using higher quality SOI wafers should solve this problem at the price of increased costs.

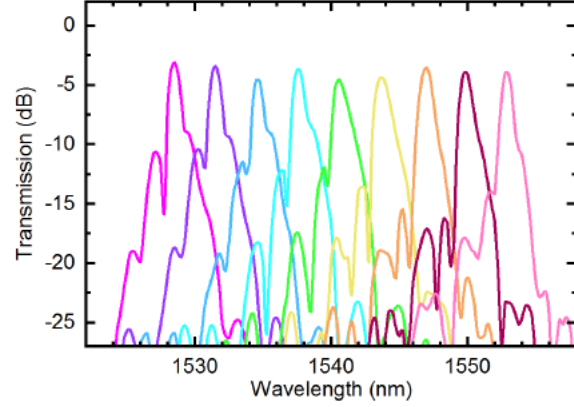


Figure 14. Transmission spectrum of a 1×9 demultiplexer as used for the on-chip WDM transmitter unit.

3.3 Thermal modulators

Thermal modulators have been intensively investigated for the purpose of working point control based on the thermo-optic effect of silicon [18]. For first studies, our thermal modulators are built as Mach-Zehnder modulators and feature 100 μm long thermal phase shifters. Their cross section is similar to the pn-phase shifters with a rib width and thickness of 500 nm and 250 nm, respectively, and a slab thickness of 120 nm. The waveguide region is p-doped homogeneously along the entire modulator with the same doping concentration as for the carrier-depletion MZMs. Current flows perpendicular to the waveguide from one slab to the other, heating the waveguide region. Although thermo-optic modulation is fairly slow compared to plasma-dispersion modulation, it is well suited for working point control with decent power requirements and footprint.

The result of an experiment measuring the optical transmission versus the electrical input power is illustrated in figure 15. With an maximum input power of 70 mW we can perform a phase shift of almost 3π . A 2π -shift is reached at a power of about 58 mW. Using a configuration with a thermo-optic phase shifter in each

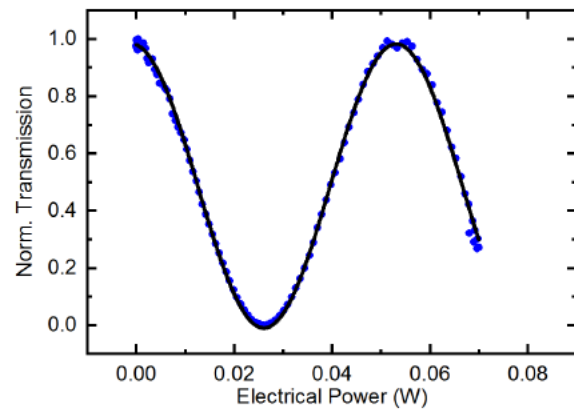


Figure 15. Normalized transmission of thermal modulator versus input electrical power.

arm of an MZM, each of them just have to be able to perform a π -shift using just 29 mW for a full 2π phase shift for complete working point control.

An optimized design with measures to insulate the waveguides thermally is expected to improve the performance of the thermal phase shifters significantly, further decreasing the required power for operating point control.

4 Conclusions and outlook

In this paper, we presented the key building blocks to construct a monolithically integrated transmitter based on silicon photonics and WDM technology. After the second chip run, all the key components of the transmitter work now. For our 3 mm long MZMs, the figure of merit $V_\pi L_\pi$ is 4.6 V·cm. And The insertion loss is 4.84 dB. Although the measured 3 dB cut-off frequency is 3.28 GHz, the characteristics is smooth enough to perform error free transmissions with a rate of 11.3 Gb/s down to driving voltages as low as 3 V. The Echelle grating (de-)multiplexers as one other key component for an integrated WDM system exhibit excellent performance with low optical loss, low crosstalk, and only a small wavelength shift due to thickness deviations of the silicon layer, which can be overcome with tighter tolerance.

For the next design, the doping will be improved and the electrode design will be optimized to achieve a better RF performance and a better impedance matching. Additionally, the thermal modulators, which showed a good performance, will be included into the high-speed MZMs to set the working point without deteriorating the modulation performance. With all key components working, irradiation tests will be performed in the near future for the system and a monolithically integrated, radiation-hardened, high-bandwidth WDM system is just around the corner.

Acknowledgments

This research is supported by the program Matter and Technology of the Helmholtz Association, Germany, and the China Scholarship Council (CSC), China.

References

- [1] L. Rossi and O. Brüning, *High Luminosity Large Hadron Collider: A description for the European Strategy Preparatory Group*, CERN-ATS-2012-236 (2012).
- [2] P. Baldwin and M. Gaillard, *CERN's IT gears up to face the challenges of LHC Run 2*, <http://cerncourier.com/cws/article/cern/65031>, 2016.
- [3] F. Vasey, *Optical links for LHC: experience from the CMS project and future prospects*, in proceedings of the 10th Workshop on Electronics for LHC and Future Experiments, Boston, MA, U.S.A., 13–17 September 2004, pp. 31–33.
- [4] CMS collaboration, *The versatile link, a common project for super-LHC*, 2009 *JINST* **4** P12003.
- [5] J. Troska, S. Detraz, S. Seif El Nasr-Storey, P. Stejskal, C. Sigaud, C. Soos et al., *Radiation damage studies of lasers and photodiodes for use in Multi-Gb/s optical data links*, *IEEE Trans. Nucl. Sci.* **58** (2011) 3103.

- [6] A. Kraxner, S. Detraz, L. Olantera, C. Scarcella, C. Sigaud, C. Soos et al., *Investigation of the Influence of Temperature and Annealing on the Radiation Hardness of Silicon Mach–Zehnder Modulators*, *IEEE Trans. Nucl. Sci.* **65** (2018) 1624.
- [7] P. Skwierawski, M. Schneider, D. Karnick, L. Eisenblätter and M. Weber, *A silicon photonic wavelength division multiplex system for high-speed data transmission in detector instrumentation*, *2016 JINST* **11** C01045.
- [8] D. Karnick, P. Skwierawski, M. Schneider, L. Eisenblätter and M. Weber, *Optical links for detector instrumentation: on-detector multi-wavelength silicon photonic transmitters*, *2017 JINST* **12** C03078.
- [9] D. Karnick, N. Bauditsch, L. Eisenblätter, T. Kühner, M. Schneider and M. Weber, *Efficient, easy-to-use, planar fiber-to-chip coupling process with angle-polished fibers*, in proceedings of the *67th Electronic Components and Technology Conference*, Orlando, FL, U.S.A., 30 May – 2 June 2017, pp. 1627–1632.
- [10] J. Ding, H. Chen, L. Yang, L. Zhang, R. Ji, Y. Tian et al., *Ultra-low-power carrier-depletion mach-zehnder silicon optical modulator*, *Opt. Expr.* **20** (2012) 7081.
- [11] R. Soref and B. Bennett, *Electrooptical effects in silicon*, *IEEE Jo. Quantum Electron.* **23** (1987) 123.
- [12] K. Cooney and F.H. Peters, *Analysis of multimode interferometers*, *Opt. Expr.* **24** (2016) 22481.
- [13] Y. Ding, C. Peucheret, H. Ou and K. Yvind, *Fully etched apodized grating coupler on the SOI platform with -0.58 dB coupling efficiency*, *Opt. Lett.* **39** (2014) 5348.
- [14] W.S. Zaoui, A. Kunze, W. Vogel, M. Berroth, J. Butschke, F. Letzkus et al., *Bridging the gap between optical fibers and silicon photonic integrated circuits*, *Opt. Expr.* **22** (2014) 1277.
- [15] Y. Zhang, M. Schneider, D. Karnick, L. Eisenblätter, T. Kühner and M. Weber, *Low-loss and robust DWDM Echelle grating (de-) multiplexers in SOI technology*, *Proc. SPIE* **10914** (2019) 109140J.
- [16] Y. Zhang, D. Karnick, M. Schneider, L. Eisenblätter, T. Kühner and M. Weber, *Concept, design and verification of components for an integrated on-detector silicon photonic multi-channel transmitter*, in proceedings of the *Topical Workshop on Electronics for Particle Physics*, Antwerpen, Belgium, 17–21 September 2018, *PoS(TWEPP2018)*057.
- [17] R.J. Lycett, D.F.G. Gallagher and V.J. Brulis, *Perfect chirped echelle grating wavelength multiplexor: Design and optimization*, *IEEE Photon. J.* **5** (2013) 2400123.
- [18] N.C. Harris, Y. Ma, J. Mower, T. Baehr-Jones, D. Englund, M. Hochberg et al., *Efficient, compact and low loss thermo-optic phase shifter in silicon*, *Opt. Expr.* **22** (2014) 10487.